Controllable synthesis of concave cubic gold core–shell nanoparticles for plasmon-enhanced photon harvesting

Yang Bai [a,1], Teera Butburee [a,1], Hua Yu [a], Zhen Li [b], Rose Amal [c], G.Q. (Max) Lu [a], Lianzhou Wang [a,*]

[a] Nanomaterials Centre, School of Chemical Engineering and AIBN, The University of Queensland, Brisbane, QLD 4072, Australia
[b] Institute of Superconducting and Electronic Materials, Australian Institute of Innovative Materials, The University of Wollongong, North Wollongong, NSW 2500, Australia
[c] School of Chemical Engineering, The University of New South Wales, Sydney, NSW 2052, Australia

ABSTRACT

Well-defined core–shell nanoparticles (NPs) containing concave cubic Au cores and TiO$_2$ shells (CA@T) were synthesized in colloidal suspension. These CA@T NPs exhibit Localized Surface Plasmon Resonance (LSPR) absorption in the NIR region, which provides a unique property for utilizing the low energy range of the solar spectrum. In order to evaluate the plasmonic enhancement effect, a variety of CA@T NPs were incorporated into working electrodes of dye-sensitized solar cells (DSSCs). By adjusting the shell thickness of CA@T NPs, the plasmonic property can be tuned to achieve maximum photovoltaic improvement. Furthermore, the DSSC cells fabricated with the CA@T NPs exhibit a remarkably plasmonic assisted conversion efficiency enhancement (23.3%), compared to that (14.8%) of the reference cells assembled with spherical Au@TiO$_2$ core–shell (SA@T) NPs under similar conditions. Various characterizations reveal that this performance improvement is attributed to the much stronger electromagnetic field generated at the hot spots of CA@T NPs, resulting in significantly higher light harvesting and more efficient charge separation. This study also provides new insights into maximizing the plasmonic enhancement, offering great potential in other applications including light–matter interaction, photocatalytic energy conversion and new-generation solar cells.

© 2014 Published by Elsevier Inc.

1. Introduction

Localized Surface Plasmon Resonance (LSPR) arising from metal nanoparticles (NPs) enables the manipulation of light at the sub-wavelength scale, by collecting oscillated conduction electrons coupling with propagating light wave in confined volume. Metallic nanomaterials with LSPR have attracted considerable scientific interest in the development of various applications, such as Surface-Enhanced Raman Spectroscopy (SERS) [1], biosensor [2], imaging [3], photocatalysis [4], and molecular electronics [5]. In recent years, LSPR of metallic nanostructures has also proven to be a promising way to further improve the performance of various solar cell configurations, e.g., silicon solar cells [6], GaAs solar cells [7], organic solar cells [8], dye-sensitized solar cells (DSSCs) [9], and perovskite solar cells [10]. By proper incorporation of metallic nanomaterials into electrodes, light can be efficiently trapped or concentrated due to the LSPR, resulting in the photovoltaic enhancement. To understand the observed improvement in power conversion efficiency (PCE), a variety of theories have been postulated and summarized as follows: (1) the local near field enhancement from surface plasmon excitation enhances charge carrier generation, resulting in the increase in photocurrent [9a,11]; (2) strong scattering of the plasmonic metals at surface plasmon wavelengths is able to re-direct light into a solar cell substrate [12]; (3) charge separation is promoted as a result of localized electromagnetic field [13].

In NPs, it is well known that the shape is as important as size in determining the plasmonic and catalytic properties of metallic NPs. To date, a number of synthetic strategies have been developed to prepare metallic NPs with various shapes, including sphere [14], cubes [15], octahedral [16], rods [17], tetrahedra [18], bipyramids [19], and newly emerged concave cubes [20]. Certain NPs with well-defined sharp corners and edges, where hot spots located, would generate much stronger electromagnetic field [20b,21] and exhibit larger plasmonic enhancement factors [22]. Among those intriguing nanostructures listed above, concave cubic NPs are the most interesting, because of their hot spots featuring intensified electromagnetic field as well as extraordinary high chemical activity originating from high-index facets. Despite such distinct optical and chemical properties of concave cubic NPs, there is no

report yet on applying such concave nanostructures in photovoltaic devices. This could be due to the challenges in synthesis [23] as well as structure stability especially in DSSC cells containing highly corrosive electrolyte.

In this work, we report a strategy for the synthesis of hot spot-containing concave cubic Au@TiO$_2$ core–shell (CA@T) NPs with precisely controlled core morphology and shell thickness using a colloidal wet-chemical approach. The hot spot-containing CA@T NPs are hypothesized to offer superior plasmonic enhancement. As discussed above, much stronger electromagnetic field is preferably induced at the sharp corners and edges of metal NPs. Therefore, more photons will be captured by hot spot-containing metal NPs resulting in more electrons generated, as compared to the normal spherical metal NPs with smooth surface (Scheme 1). To confirm our idea and evaluate the plasmonic enhancement effect, such hot spots-containing core–shell NPs were incorporated into the working electrodes of DSSCs. Systematic study shows that optimal shell thickness of CA@T NPs is crucial in achieving maximum photovoltaic enhancement. More importantly, plasmonic assisted conversion efficiency enhancement (23.3%) was observed in the DSSC cells with hot spots-containing CA@T NPs, compared to that (14.8%) of the reference cells incorporating spherical Au@TiO$_2$ core–shell (SA@T) NPs with comparable core size and shell thickness under the same testing conditions. This confirms our hypothesis and the feasibility of using new hot spot-containing CA@T NPs to maximize the plasmonic enhancement in photovoltaic devices.

2. Experimental

2.1. Concave cubic Au@TiO$_2$ synthesis

Concave nanocubic Au with well-defined sharp corners and edges and the spherical Au nanoparticles for comparison were synthesized using a modified colloidal wet-chemical method [24]. The well-defined CA@T NPs were synthesized according to the technique we developed previously [25]. Firstly, 500 mL of as-prepared Au nanoparticle suspension was centrifuged and washed by DI water for 3 cycles. The particles were then re-dispersed in 25 mL DI water. Afterwards, 25 mL of 50 mM thioglycolic acid was added to the solution and stirred overnight to change the functional group of the metal's surface to be preferable to TiO$_2$ deposition. The pH values of both Au-core solution and 25 mL of 0.5 M TiCl$_3$ precursor solution were adjusted to 2.25 by NH$_4$OH. The TiCl$_3$ precursor solution was then added to the Au core solution under mechanical stirring. The pH of the reaction was kept at 2.25 ± 0.05 throughout the reaction by dropping 1 M NH$_4$OH when the pH decreased. The TiO$_2$ shell thickness could be tuned by controlling the reaction time. After desirable deposition time, the reaction was stopped by

centrifugation at 6000 rpm. The top aliquot was poured to remove the exceed TiCl$_3$ precursor, and the NPs were re-dispersed, washed and centrifuged for 3 times, then dried at 60 °C for 24 h before use. The concave cubic Au@TiO$_2$ core–shell NPs with four different shell thicknesses were denoted as CA@T-1, CA@T-2, CA@T-3, and CA@T-4, respectively, whist the spherical Au@TiO$_2$ core–shell NP was named as SA@T.

2.2. Electrode preparation

To prepare the DSSC working electrodes, FTO substrates (2.2 mm thickness, 7–8 Ω/sq, OPV-FT022-7, OPVT-Yingkou) was cleaned with acetone and 2-propanol using an ultrasonic bath for 30 min, respectively, and then thoroughly rinsed with distilled water. The pastes incorporating various Au@TiO$_2$ NPs were prepared with a modified procedure [26]. The ratio of Au@TiO$_2$ NPs to P25 was 0.7 wt%. The working electrode films were fabricated by the doctor-blading method using P25 pastes and P25 pastes incorporating Au@TiO$_2$ NPs as described in our previous work [27]. The working electrodes were then put into a muffle furnace and gradually heated at 325 °C for 5 min, at 375 °C for 5 min, at 450 °C for 15 min, and at 500 °C for 15 min. The resultant working electrodes prepared from P25 paste and P25 incorporating core–shell NPs (CA@T-1, CA@T-2, CA@T-3, CA@T-4, and SA@T) were denoted as P25, C1, C2, C3, C4, and S, respectively. Finally, all the electrodes were post-treated again with TiO$_2$ organic sol and annealed at 450 °C again [28]. After cooling to 80 °C, the TiO$_2$ films were immersed into a 0.5 mM solution of N719 dye (Dyesol) in a mixture of acetonitrile/tert-butanol (V/V = 1/1) for 12–14 h [28,29].

2.3. Cell fabrication

The dye-loaded working electrodes and Pt counter electrodes (OPVT-Yingkou) were assembled into a sandwich type cell and sealed with a spacer of 60 μm thickness (OPV-Surlyn-60, OPVT-Yingkou) with a drop of the I^-/I_3^- organic solvent based electrolyte solution (EL-HPE, Dyesol) introduced via vacuum back-filling [30]. The sealed DSSCs were used for the photocurrent–voltage testing with an active area of 0.16 cm^2.

2.4. Characterization and measurements

The morphology of Au NPs and core–shell NPs were examined by transmission electron microscopy (TEM, JEOL 1010). The absorption properties of core–shell NPs dispersed in ethanol and dye-sensitized photoelectrodes containing core–shell NPs were investigated by UV–visible light spectrometer (Shimadzu UV-2450). The photocurrent–voltage (J–V) tests of DSSCs were
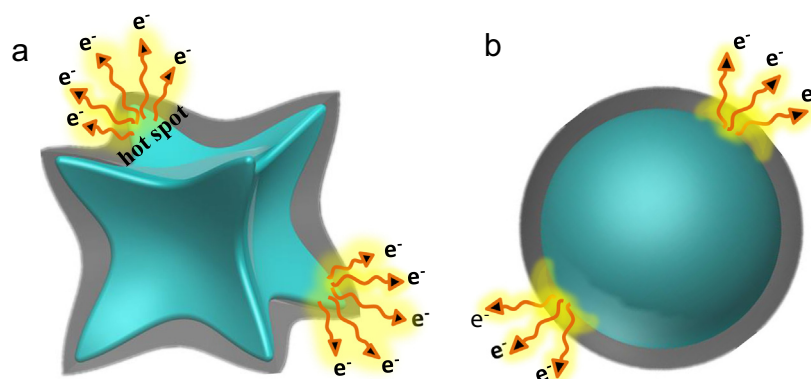
Scheme 1. Schematic illustration of superior LSPR effect induced by (a) hot spot-containing concave cubic Au@TiO$_2$ core–shell (CA@T) NP in comparison with (b) normal spherical Au@TiO$_2$ core–shell (SA@T) NP.

performed under one sun condition using an AM 1.5 solar simulator (Oriel) and recorded by a Keithley model 2420 digital source meter. The incident photon-to-current conversion efficiency (IPCE) plotted as a function of the excitation wavelength was obtained by using a Newport 1918-c power meter under irradiation of a 300 W Oriel xenon light source with an Oriel Cornerstone 260 1/4 m monochromator in direct-current mode. The electrochemical impedance spectra (EIS) were measured under one sun illumination over a frequency range of 10^5–0.1 Hz by using Solartron 1260 Frequency Response Analyzer in combination with a Solartron 1480 Potentiostat. The applied bias voltage and ac amplitude were set as open circuit voltage and 10 mV, respectively. The time-resolved fluorescence emission decay spectra of various dye-sensitized TiO_2 films on cover glasses were monitored at 532 nm by using the fluorescence spectrometer (FLS 920, Edinburgh Instruments).

3. Results and discussion

To synthesize CA@T NPs, we first prepared concave cubic Au NPs using a modified method [24b]. As shown in the TEM images (Fig. 1a and b), it is clear that each face of the nanocubic Au was excavated by a square pyramid in the center. The nanocubes exhibited a darker contrast in the center than at the edges, which confirms the formation of a concave structure. The average edge length of concave nanocubes was determined to be *ca.* 52 nm (Fig. 1b). After functionalization of Au-cores by using thioglycolic acid, $TiCl_3$ precursor solution was added to form a TiO_2 layer on the surface of Au-cores in a controllable manner (see Section 2). Representative TEM images of various CA@T NPs are shown in Fig. 1(c–j). It can be clearly seen that the cores have well-defined concave nanocubic geometry and well covered by the TiO_2 shells with increasing thickness of roughly 2, 7, 14, and 43 nm.

To better understand the hot spot effect, spherical Au NPs (S-Fig. 1a and b) with smooth surfaces and comparable particle size were synthesized using previously reported method [24a]. SA@T NPs with a selective shell thickness of *ca.* 7 nm shown in S-Fig. 1c and d were then prepared for a fair comparison with CA@T-2 in terms of plasmonic property.

Fig. 2 shows the absorption spectra of CA@T and SA@T NPs well-dispersed in ethanol. The absorption peak of SA@T NPs is located at 601 nm in the visible region, whilst CA@T NPs exhibit red-shifted
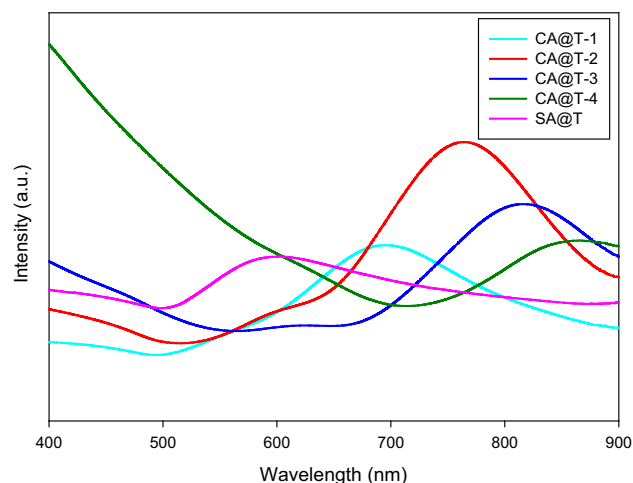

Fig. 2. Absorption spectra of CA@T and SA@T NPs well-dispersed in ethanol.

surface plasmon absorption with absorption peaks at 695 nm (CA@T-1), 765 nm (CA@T-2), 816 nm (CA@T-3), and 865 nm (CA@T-4) in the near infrared (NIR) region, respectively. In the case of CA@T NPs, the absorption peak shifts from 695 nm to longer wavelengths up to 865 nm with increasing TiO_2 shell thickness, due to the higher dielectric constant surrounding the Au cores. The NIR absorption of CA@T NPs from LSPR provides a unique opportunity for utilizing the low energy range of solar spectrum.

In order to study the plasmonic property and evaluate the hot spot-effect of CA@T NPs, they have been incorporated into the working electrodes of DSSCs (see Section 2). Reference DSSC devices were fabricated using bare P25 films. We first investigated the influence of shell thickness of CA@T NPs on the plasmonic enhancement effect in DSSCs. Fig. 3 shows the photocurrent density–voltage (*J*–*V*) curves of the DSSCs with P25, C1, C2, C3, C4, and S working electrodes under standard simulated AM 1.5 illumination. The corresponding photovoltaic performance parameters are tabulated in Table 1 for easy comparison. The DSSC cells fabricated with pure P25 working electrodes exhibited a short-current density (J_{sc}) of 14.78 mA cm^{-2}, open-circuit voltage (V_{oc}) of 753 mV, and fill factor (*FF*) of 0.662, yielding overall power conversion efficiency (η) of 7.37%. With the incorporation of CA@T-1.
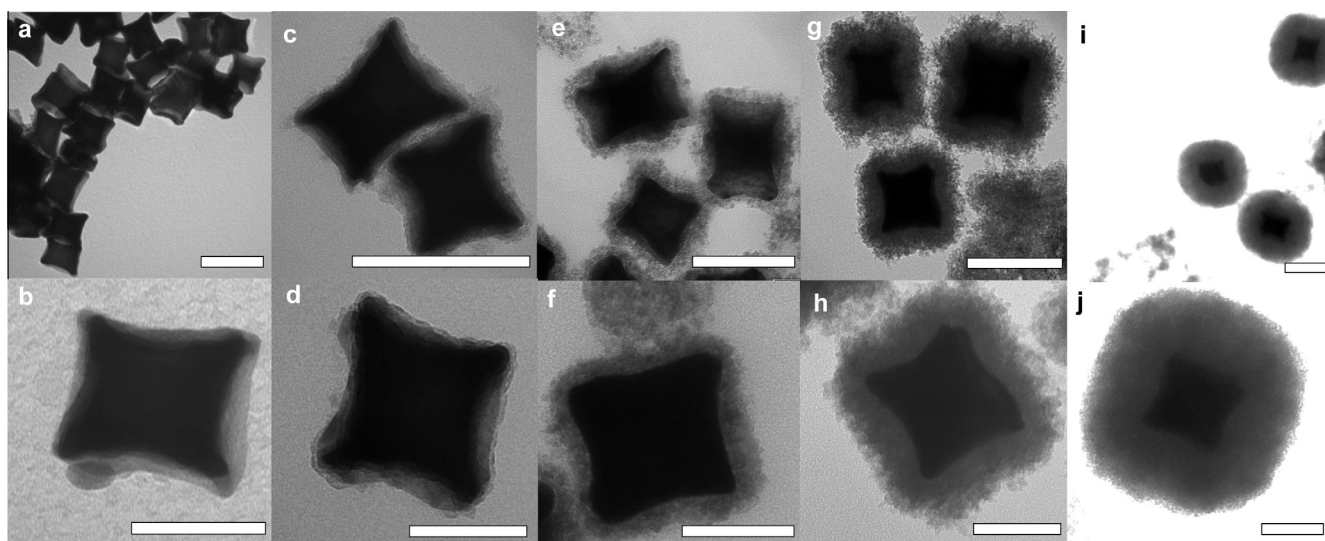

Fig. 1. TEM images of concave cubic Au NPs (a and b) and C-Au@T NPs with increasing shell thickness [CA@T-1 (c and d), CA@T-2 (e and f), CA@T-3 (g and h) and CA@T-4 (i and j)] Bottom panels show the zoomed-in images of NPs in the corresponding top panels. Scale bars for top and bottom panels are 100 and 50 nm, respectively.
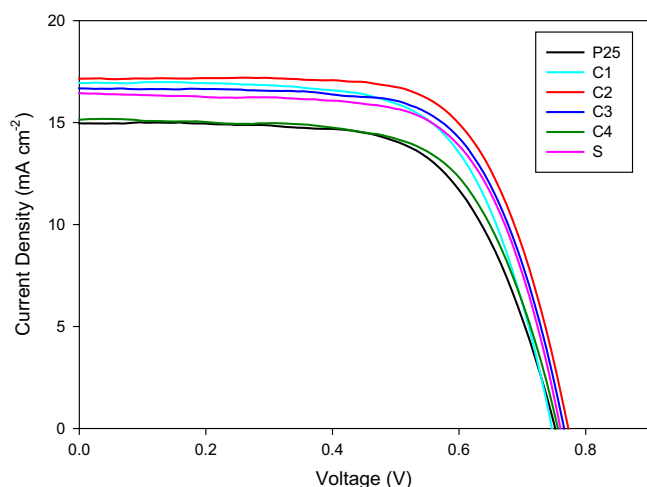
Fig. 3. Photocurrent density–voltage characteristics of DSSCs based on a variety of working electrodes, measured at AM1.5 illumination (100 mW cm^{-2}).

Table 1
Photovoltaic performance of DSSCs with different working electrodes.

Samples	J_{sc} (mA cm^{-2})	V_{oc} (mV)	FF (%)	η (%)
P25	14.78	753	66.2	7.37
C1	17.08	747	66.4	8.47
C2	17.25	775	68.0	9.09
C3	16.73	768	68.5	8.80
C4	15.16	763	66.5	7.63
S	16.43	762	67.6	8.46

J_{sc}: short-circuit current density, V_{oc}: open-circuit voltage, FF: fill factor, η: energy conversion efficiency; the average value of each data was obtained by testing at least 8 cells.

NPs into the working electrodes (C1), PCE significantly increased to 8.47% which is mainly attributed to the largely improved J_{sc} of 17.08 mA cm^{-2}, nevertheless V_{oc} slightly decreased to 747 mV. PCE was further increased to 9.09% when CA@T-2 NPs with larger shell thickness of 6.6 nm were doped into the working electrodes, corresponding to an efficiency improvement of 23.3%. It can be seen that the enhancement in all performance parameters including J_{sc} (17.25 mA cm^{-2}), V_{oc} (775 mV), and FF (0.68) is responsible for the further improved PCE. When the TiO$_2$ shell thickness reaches 13.8 nm (CA@T-3) and 43.5 nm (CA@T-4), the photocurrent of DSSCs fabricated with CA@T-3 and CA@T-4 NPs decreased to 16.73 and 15.16 mA cm^{-2}, resulting in lower PCE of 8.8% and 7.63%, respectively, as compared to the cells containing CA@T-2 NPs. Such an observation reveals that the thickness of semiconducting shell plays an important role in tuning and maximizing the plasmonic enhancement effect in DSSCs. When the shell is super thin with a thickness of only ca. 2 nm (CA@T-1), it may be hard to maintain the complete core–shell structure and fully cover the metal core upon annealing. Then the exposed Au surface would trap both electron and holes and thus serve as recombination sites, resulting in the decrease of V_{oc} in DSSCs. Slightly increasing the shell thickness to ca. 7 nm ensures the stability of core–shell NPs, and an improved V_{oc} as well as a slightly increased FF was obtained as a result of the charge equilibrium between the metal cores and the surrounding TiO$_2$ materials. Nonetheless, further increasing the shell thickness would keep the sensitizer molecules too far from the cores and weaken the LSPR enhancement effect, thus reducing the photocurrent in DSSCs. In addition, the control experiment with SA@T NPs exhibited a relatively lower PCE of 8.46% in comparison with CA@T-2 NPs, despite the comparable TiO$_2$ shell thickness. Obviously, the superior photovoltaic enhancement achieved

is attributed to the stronger LSPR effect generated at the hot spots of CA@T-2 NPs as shown in Scheme 1.

The absorption spectra of various dye-loaded working electrodes shown in Fig. 4 were conducted to explore the mechanism behind the plasmonic enhancement in DSSCs. Despite the similar amount of dye-loading in all these films, the presence of CA@T NPs seems to have a noticeable effect on the dye absorption property. Compared to the pristine P25 films, the dye molecules adsorbed on P25 films incorporated with CA@T as well as SA@T NPs exhibited significantly higher loading, which is beneficial to the photocurrent increase in DSSCs. This enhancement of dye extinction could be attributed to the interaction of dye molecular dipole and enhanced electromagnetic field induced by LSPR, together with the increase of light scattering which prolonged the optical path [9b]. In spite of comparable metal core size and shell thickness, the absorption of SA@T sample is considerably lower than that of hot spot-containing CA@T-2. The trend of absorption enhancement is obviously consistent with that of photocurrent increase (Table 1).

The IPCE spectra of DSSCs fabricated with various working electrodes provide further evidence on the plasmonic enhancement effect of CA@T NPs. The IPCE can be rationalized using the following Eq. (1) [27,31]:

$$IPCE(\lambda) = A\varphi_{inj}\eta_{coll} \qquad (1)$$

where A is the light harvesting efficiency of the dye molecules, φ_{inj} is the electron injection efficiency, and η_{coll} is the electron collection efficiency. As shown in Fig. 5, the improvement of the IPCE value is achieved over the whole excitation spectrum of the N719 dyes, and highly corresponds to the absorption enhancement in Fig. 4. In plasmon-enhanced DSSC cells, plasmon excitation could improve optical density surrounding the metal NPs and the dye sensitizer located in the vicinity of plasmonic core–shell NPs especially the hot spot-containing CA@T NPs could capture more photons and generate more electrons (Scheme 1), thus increasing IPCE [32].

Electrochemical impedance spectra (EIS) were collected to further investigate the influence of localized electromagnetic field induced by CA@T NPs on charge separation and electron lifetime in DSSCs. Fig. 6a shows the Nyquist plots of DSSCs based on a variety of working electrodes measured at open-circuit voltage under illumination and the equivalent circuit is depicted as its inset. In general, three semicircles could be obtained in the Nyquist plot of DSSCs, which are assigned to (1) the redox reaction at the platinum counter electrode/electrolyte interface at high frequencies
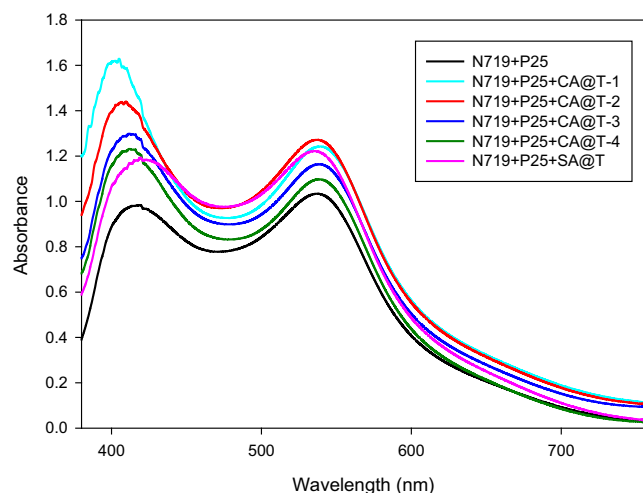

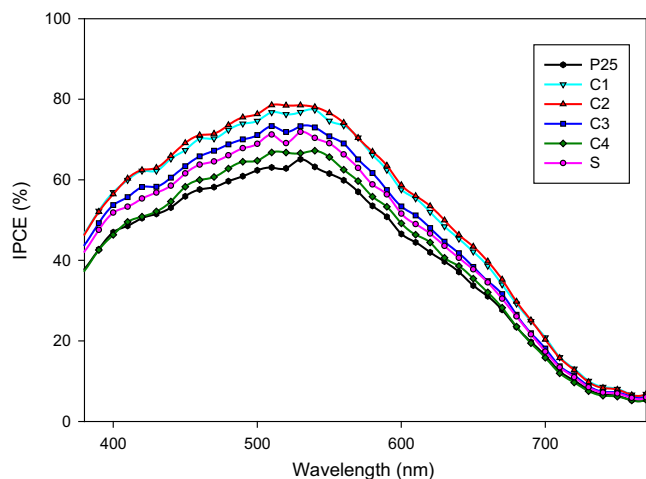Fig. 4. Absorption spectra of various dye-loaded working electrode films.

Fig. 5. IPCE spectra of DSSCs based on a variety of working electrodes.

Fig. 7. Fluorescence emission decay spectra of the N719 dye loaded on cover glass coated with P25 film and P25 films incorporating CA@T and SA@T NPs.
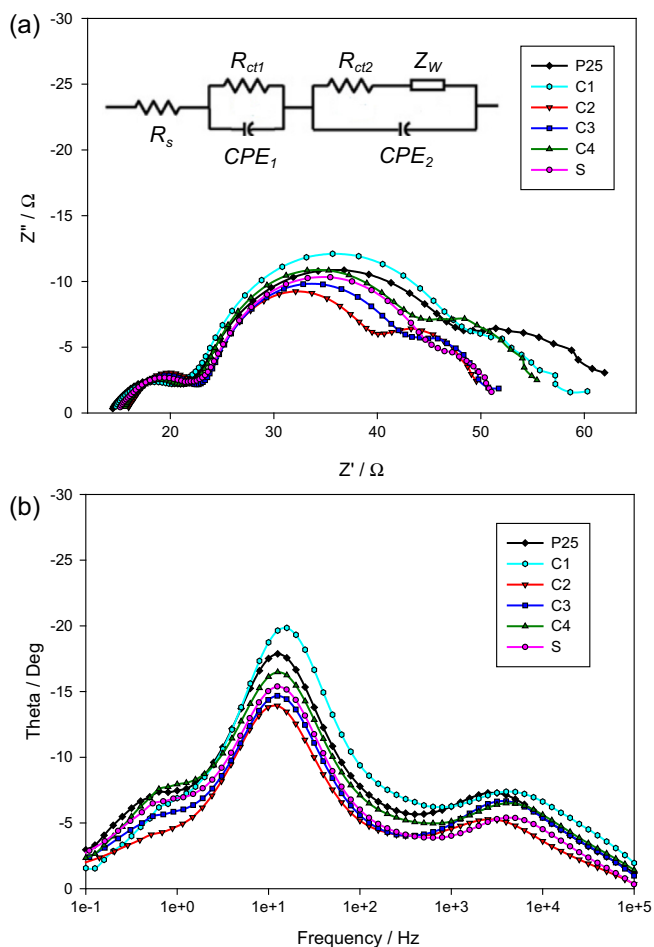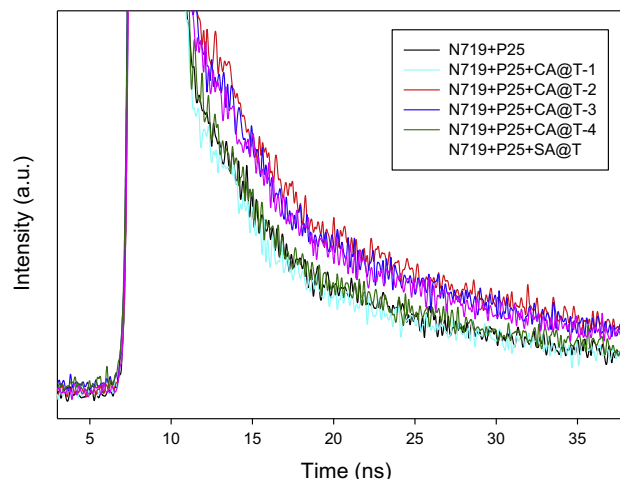

Fig. 6. (a) Nyquist plots and (b) corresponding Bode phase plots of the DSSC cells fabricated with various working electrodes. The inset shows the equivalent circuit.

restrained with the incorporation of CA@T NPs and the cells containing CA@T-2 showed the most efficient electron transport in terms of the smallest R_{ct2}. This result reveals that the shell thickness is vital in tuning the property of core–shell NPs, and more importantly the stronger electromagnetic field induced on hot spots is of benefit to facilitating more efficient charge separation, thus suppressing recombination. The electron lifetime (τ_e) can be calculated according to Eq. (2):

$$\tau_e = \frac{1}{2\pi\omega_{max}} \tag{2}$$

where ω_{max} is the maximum frequency from the intermediate Nyquist semicircle [34]. As shown in Bode phase plots (Fig. 6b), the medium-frequency peaks (ω_{max}) are in the same order of C2 < C3 < S < C4 < P25 < C1. The significantly decreased ω_{max} in DSSCs containing CA@T-2 NPs suggests prolonged electron lifetime, which well explains the improvement of V_{oc} observed in Fig. 3.

To further confirm the facilitated charge separation and increased electron lifetime, we investigated the decay behavior of the photoexcited carriers. Fig. 7 shows the time-resolved fluorescence emission decay spectra for N719 dye loaded on cover glass coated with both pure P25 film and P25 films incorporating CA@T and SA@T NPs. Except C1, the decay kinetics of films C2, C3, C4, and S become slow, in contrast to the decay curve of pristine P25 film. In detail, the decay lifetime of carriers for pristine P25 film is *ca.* 12.2 ns while those of C2, C3, C4, and S increase to 15.2, 14.6, 12.4, and 13.7 ns. Nevertheless, the carrier decay lifetime for C1 reduces to 11.2 ns. This indicates that by optimizing the shell thickness, plasmonic core–shell NPs could significantly promote the charge separation, thus suppressing the recombination of the photogenerated carriers and the backward transport of electrons from TiO$_2$ to the electrolyte. Moreover, the core–shell NPs containing hot spots are expected to maximize the photovoltaic enhancement as they can not only capture more photons but also facilitate more efficient charge separation owing to the much stronger localized electromagnetic field.

4. Conclusions

In summary, we have developed a strategy for the synthesis of hot spot-containing concave cubic Au@TiO$_2$ core–shell (CA@T) NPs with precisely controlled core morphology and shell thickness, which were subsequently incorporated to form new photoanodes in DSSCs. Our studies revealed that the hot spots play an important

(R_{ct1}), (2) the electron transfer at the TiO$_2$/dye/electrolyte interface at medium frequencies (R_{ct2}), and (3) the Warburg diffusion process of I^-/I_3^- in the electrolyte at low frequency (Z_w) [33]. The diameters of the medium-frequency semicircles are in the order of C2 < C3 < S < C4 < P25 < C1 as observed in Fig. 6a. The smaller diameters indicate the lower electron transfer resistance (R_{ct2}). Therefore, other than DSSCs with CA@T-1, the recombination was

role in amplifying the performance improvement owing to the much stronger electromagnetic field surrounding CA@T-2 NPs. UV–vis absorption together with IPCE shows the significantly higher light harvesting efficiency as the extinction rate of dye molecules increases. Furthermore, the prolonged electron lifetime is confirmed by EIS and fluorescence emission decay spectra as a result of more efficient charge separation and suppressed electron recombination. The present study of well-defined hot spot-containing CA@T NPs provides new insights on maximizing the plasmonic-assisted efficiency enhancement, and could lead to new applications including nanoscale light–matter interaction, solar-to-chemical energy conversion and new-generation perovskite solar cells.

Appendix A. Supplementary material

Supplementary data associated with this article can be found, in the online version, at http://dx.doi.org/10.1016/j.jcis.2014.11.035.

References

[1] W. Wei, S. Li, J.E. Millstone, M.J. Banholzer, X. Chen, X. Xu, G.C. Schatz, C.A. Mirkin, Angew. Chem. Int. Ed. 48 (2009) 4210.
[2] (a) K.A. Willets, R.P. Van Duyne, Annu. Rev. Phys. Chem. 58 (2007) 267;
(b) J.N. Anker, W.P. Hall, O. Lyandres, N.C. Shah, J. Zhao, R.P. Van Duyne, Nat. Mater. 7 (2008) 442;
(c) A.R. Ferhan, L. Guo, D.-H. Kim, Langmuir 26 (2010) 12433.
[3] (a) L.K. Gifford, I.E. Sendroiu, R.M. Corn, A. Lupták, J. Am. Chem. Soc. 132 (2010) 9265;
(b) J.-L. Li, M. Gu, Biomaterials 31 (2010) 9492.
[4] (a) Z.W. Seh, S. Liu, M. Low, S.-Y. Zhang, Z. Liu, A. Mlayah, M.-Y. Han, Adv. Mater. 24 (2012) 2310;
(b) Z. Bian, J. Zhu, F. Cao, Y. Lu, H. Li, Chem. Commun. (2009) 3789;
(c) W. Hou, S.B. Cronin, Adv. Funct. Mater. 23 (2013) 1612.
[5] (a) X. Chen, Y.-M. Jeon, J.-W. Jang, L. Qin, F. Huo, W. Wei, C.A. Mirkin, J. Am. Chem. Soc. 130 (2008) 8166;
(b) P. Banerjee, D. Conklin, S. Nanayakkara, T.-H. Park, M.J. Therien, D.A. Bonnell, ACS Nano 4 (2010) 1019.
[6] S. Pillai, K. Catchpole, T. Trupke, M. Green, J. Appl. Phys. 101 (2007) 093105.
[7] K. Nakayama, K. Tanabe, H.A. Atwater, Appl. Phys. Lett. 93 (2008) 121904.
[8] (a) X. Li, W.C.H. Choy, L. Huo, F. Xie, W.E.I. Sha, B. Ding, X. Guo, Y. Li, J. Hou, J. You, Y. Yang, Adv. Mater. 24 (2012) 3046;
(b) A.J. Morfa, K.L. Rowlen, T.H. Reilly, M.J. Romero, J. van de Lagemaat, Appl. Phys. Lett. 92 (2008) 013504.
[9] (a) M.D. Brown, T. Suteewong, R.S.S. Kumar, V. D'Innocenzo, A. Petrozza, M.M. Lee, U. Wiesner, H.J. Snaith, Nano Lett. 11 (2010) 438;
(b) H. Choi, W.T. Chen, P.V. Kamat, ACS Nano 6 (2012) 4418;
(c) S. Chang, Q. Li, X. Xiao, K.Y. Wong, T. Chen, Energy Environ. Sci. 5 (2012) 9444;
(d) M.K. Gangishetty, K.E. Lee, R.W.J. Scott, T.L. Kelly, ACS Appl. Mater. Interfaces 5 (2013) 11044.
[10] W. Zhang, M. Saliba, S.D. Stranks, Y. Sun, X. Shi, U. Wiesner, H.J. Snaith, Nano Lett. 13 (2013) 4505.
[11] (a) N.C. Jeong, C. Prasittichai, J.T. Hupp, Langmuir 27 (2011) 14609;
(b) C. Hägglund, M. Zäch, B. Kasemo, Appl. Phys. Lett. (2008) 92.
[12] (a) D. Derkacs, S.H. Lim, P. Matheu, W. Mar, E.T. Yu, Appl. Phys. Lett. (2006) 89;
(b) H.A. Atwater, A. Polman, Nat. Mater. 9 (2010) 205.
[13] (a) Y. Tian, T. Tatsuma, J. Am. Chem. Soc. 127 (2005) 7632;
(b) L. Du, A. Furube, K. Yamamoto, K. Hara, R. Katoh, M. Tachiya, J. Phys. Chem. C 113 (2009) 6454;
(c) P. Reineck, G.P. Lee, D. Brick, M. Karg, P. Mulvaney, U. Bach, Adv. Mater. 24 (2012) 4750.
[14] S.D. Perrault, W.C.W. Chan, J. Am. Chem. Soc. 131 (2009) 17042.
[15] F.-R. Fan, D.-Y. Liu, Y.-F. Wu, S. Duan, Z.-X. Xie, Z.-Y. Jiang, Z.-Q. Tian, J. Am. Chem. Soc. 130 (2008) 6949.
[16] C. Li, K.L. Shuford, Q.H. Park, W. Cai, Y. Li, E.J. Lee, S.O. Cho, Angew. Chem. 119 (2007) 3328.
[17] J. Zhang, M.R. Langille, C.A. Mirkin, Nano Lett. 11 (2011) 2495.
[18] B. Wiley, T. Herricks, Y. Sun, Y. Xia, Nano Lett. 4 (2004) 1733.
[19] M.L. Personick, M.R. Langille, J. Zhang, N. Harris, G.C. Schatz, C.A. Mirkin, J. Am. Chem. Soc. 133 (2011) 6170.
[20] (a) J. Zhang, M.R. Langille, M.L. Personick, K. Zhang, S. Li, C.A. Mirkin, J. Am. Chem. Soc. 132 (2010) 14012;
(b) M. Rycenga, M.R. Langille, M.L. Personick, T. Ozel, C.A. Mirkin, Nano Lett. 12 (2012) 6218.
[21] (a) L.J. Sherry, S.-H. Chang, G.C. Schatz, R.P. Van Duyne, B.J. Wiley, Y. Xia, Nano Lett. 5 (2005) 2034;
(b) M. Haggui, M. Dridi, J. Plain, S. Marguet, H. Perez, G.C. Schatz, G.P. Wiederrecht, S.K. Gray, R. Bachelot, ACS Nano 6 (2012) 1299.
[22] M.J. Banholzer, J.E. Millstone, L. Qin, C.A. Mirkin, Chem. Soc. Rev. 37 (2008) 885.
[23] X. Huang, Z. Zhao, J. Fan, Y. Tan, N. Zheng, J. Am. Chem. Soc. 133 (2011) 4718.
[24] (a) C. Ziegler, A. Eychmüller, J. Phys. Chem. C 115 (2011) 4502;
(b) M.L. Personick, M.R. Langille, J. Zhang, C.A. Mirkin, Nano Lett. 11 (2011) 3394.
[25] T. Butburee, Y. Bai, J. Pan, X. Zong, C. Sun, G. Liu, L.J. Wang, Mater. Chem. A 2 (2014) 12776.
[26] S. Ito, P. Chen, P. Comte, M.K. Nazeeruddin, P. Liska, P. Péchy, M. Grätzel, Prog. Photovolt. Res. Appl. 15 (2007) 603.
[27] Y. Bai, H. Yu, Z. Li, R. Amal, G.Q. Lu, L.Z. Wang, Adv. Mater. 24 (2012) 5850.
[28] Y. Bai, Z. Xing, H. Yu, Z. Li, R. Amal, L. Wang, ACS Appl. Mater. Interfaces 5 (2013) 12058.
[29] Y. Bai, X. Zong, H. Yu, Z.-G. Chen, L. Wang, Chem. Eur. J. 20 (2014) 8670.
[30] S. Ito, T.N. Murakami, P. Comte, P. Liska, C. Grätzel, M.K. Nazeeruddin, M. Grätzel, Thin Solid Films 516 (2008) 4613.
[31] (a) I. Bedja, P.V. Kamat, X. Hua, A.G. Lappin, S. Hotchandani, Langmuir 13 (1997) 2398;
(b) H. Yu, S.Q. Zhang, H.J. Zhao, G. Will, P. Liu, Electrochim. Acta 54 (2009) 1319.
[32] (a) I.K. Ding, J. Zhu, W. Cai, S.-J. Moon, N. Cai, P. Wang, S.M. Zakeeruddin, M. Grätzel, M.L. Brongersma, Y. Cui, M.D. McGehee, Adv. Energy Mater. 1 (2011) 52;
(b) B. Ding, B.J. Lee, M. Yang, H.S. Jung, J.-K. Lee, Adv. Energy Mater. 1 (2011) 415;
(c) J. Qi, X. Dang, P.T. Hammond, A.M. Belcher, ACS Nano 5 (2011) 7108.
[33] (a) Q. Wang, J.-E. Moser, M. Grätzel, J. Phys. Chem. B 109 (2005) 14945;
(b) K. Park, Q.F. Zhang, B.B. Garcia, G.Z. Cao, J. Phys. Chem. C 115 (2011) 4927;
(c) X.D. Li, D.W. Zhang, S. Chen, Z.A. Wang, Z. Sun, X.J. Yin, S.M. Huang, Mater. Chem. Phys. 124 (2010) 179;
(d) T. Hoshikawa, M. Yamada, R. Kikuchi, K. Eguchi, J. Electroanal. Chem. 577 (2005) 339.
[34] Q. Zheng, H. Kang, J. Yun, J. Lee, J.H. Park, S. Baik, ACS Nano 5 (2011) 5088.